Near-zero negative real permittivity in far ultraviolet: Extending plasmonics and photonics with B1-MoN_x

*Spyros Kassavetis[1], Brian D. Ozsdolay[2], Nikolaos Kalfagiannis[3], Adela Habib[2], Jean-Hervé Tortai[4], Sit Kerdsongpanya[2], Ravishankar Sundararaman[2], Michel Stchakovsky[5], Dimitris V. Bellas[6], Daniel Gall[2], and Panos Patsalas[1,]**

[1]Aristotle University of Thessaloniki, Department of Physics, GR-54124 Thessaloniki, Greece

[2]Rensselaer Polytechnic Institute, Department of Materials Science and Engineering, Troy, NY 12180, USA

[3]Nottingham Trent University, School of Science and Technology, Nottingham, NG11 8NS, United Kingdom

[4]University Grenoble Alpes; CNRS, CEA/LETI Minatec, Laboratoire des Technologies de la Microélectronique, F-38054 Grenoble Cedex, France

[5]HORIBA Scientific, Avenue de la Vauve, Passage Jobin Yvon, 91120, Palaiseau, France

[6]University of Ioannina, Department of Materials Science and Engineering, GR-45110 Ioannina, Greece

*e-mail: ppats@physics.auth.gr

Abstract

CMOS-compatible, refractory conductors are emerging as the materials that will advance novel concepts into real, practical plasmonic technologies. From the available pallet of materials, those with negative real permittivity at very short wavelengths are extremely rare; importantly they are vulnerable to oxidation – upon exposure to far UV radiation – and non-refractory. Epitaxial, substoichiometric, cubic MoN (B1-MoN_x) films exhibit resistivity as low as 250 μΩcm and negative real permittivity for experimental wavelengths as short as 155 nm, accompanied with unparalleled chemical and thermal stability, are reported herein. Finite-difference time domain calculations suggest that B1-MoN_x operates as an active plasmonic element deeper in the UV (100-200 nm) than any other known material, apart from Al, while being by far more stable and abundant than any other UV plasmonic conductor. Unexpectedly, the unique optical performance of B1-MoN_x is promoted by nitrogen vacancies, thus changing the common perception on the role of defects in plasmonic materials.

TOC Graphic

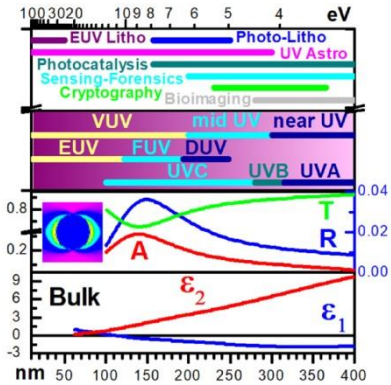

Keywords

Plasmonics; Photonics; Ultraviolet; Dielectric function; Nitrides

Introduction

In the quest of alternative plasmonic and photonic materials, the nitrides of the transition metals (TMN) of the groups IV_b-VI_b of the periodic table of elements have emerged as competitive candidates[1-7] due to their refractory character, which provides photothermal stability upon exposure to intense electric fields[4], and compatibility of their growth processes with CMOS technology[5]. Among them, TiN, ZrN and TaN are the most widely studied[1-5]; the former exhibits Localized Surface Plasmon Resonance (LSPR) in the visible range[2,3,5], while the latter in the near ultraviolet (UV) range[5,6].

The UV electromagnetic radiation that is spanning from 400 to 30 nm has a wide variety of applications, which include lithography for the fabrication of nanoelectronic and nanophotonic devices, photocatalysis, UV radioastronomy, sensing for biology, medicine and forensics, as well as cryptography and authentication via fluorescence. The materials that may operate as dielectrics, semiconductors and conductors in UV (especially in the mid-UV and vacuum-UV ranges) are exceptionally scarce due to the very high energy of UV photons, as shown in Figure 1. Especially for conductors, the list of UV actors becomes exceptionally thin due to a combination of factors, such as: 1) very few materials exhibit negative values of the real permittivity (ε_1) in the UV range, which is the most essential property for an optical conductor[5], 2) due to the high energy of UV photons many metals oxidize upon exposure to UV light[8], and 3) non-refractory metal nanostructures cannot endure intense UV beams as they melt due to the high energy of UV photons[9]. Consequently, only a handful of metals are reported to act as UV plasmonic conductors, primarily Mg (at 380 nm)[10], Al (up to 300 nm)[11], Ru (at 250 nm)[12], and Rh (at 195 nm)[13], and secondarily Ga and Sn[14], albeit with severe drawbacks such as chemical (Mg, Al, Sn) and/or thermal instability (Mg, Al, Ga, Sn), or scarcity (Ru and Rh) that strongly reduce their perspectives for realistic devices. Other metals

are not efficient optical conductors, *i.e.* they do not exhibit negative ε_1, in the UV and visible ranges due to the shallow *d*-states that result in optical interband transition in the visible or near UV range. Characteristic are the transition metals of the groups IVb-Vb-VIb (Ti, Zr, Hf, V, Nb, Ta, Cr, Mo, W)[5]. Hence, only metals with no *d*-valence electrons (such as Al and Mg), or with deep *d*-states (such as Ag and Au) exhibit negative ε_1 in optical wavelengths; a major exception is the metals of the Pt group (Ru, Os, Rh, Ir, Pd, Pt) whose *d*-states are exceptionally shallow rendering positive ε_1 values in the infrared, which become negative in optical (visible and UV) wavelengths[15].

The bonding of N*2p* electrons with the *d*-valence electrons of the transition metals of the groups IVb-Vb-VIb in TMN result in substantial shift of the *d*-states far below the Fermi level and consequently to a substantial blueshift of the optical interband transitions to UV range[5]; the resulting conduction electron densities of TMNs and their deep *d*-states suggest that TMNs should be superior as UV conductors compared to other types of ceramic conductors, such as transparent conductive oxides[2], transition metal carbides[16] and silicides[17], 2D MXenes[18], *etc*. Among the various TMNs the cubic B1-WN and B1-MoN were predicted to be the most efficient UV conductors, based on their experimental electron density values[19], and the detailed calculations of the electron density of states of the valence band (VBEDOS)[16]. However, this prediction was not confirmed for B1-WN, as epitaxial WN_x was recently found to exhibit excessive electron losses, due to the existence of both cation and anion vacancies, and the consequent deviations from stoichiometry, which result in positive values of the real permittivity in the entire visible and UV ranges[20]. On the other hand, B1-MoN was hardly stabilized in the cubic B1 structure so far and a variety of competitive MoN phases exist[21]. Although MoN_x ($x<1$) films of various phases of MoN were reported to be grown by a variety of vapor techniques[5], only recently stable epitaxial cubic B1-MoN_x films were developed[22]. Epitaxial MoN can be stabilized in the cubic structure by the incorporation

of both anion and cation vacancies[22, 23] that affect their stoichiometry[22] similar to cubic WN_x. MoN is a paramagnetic and superconducting[24] nitride of high melting point (1750 ^oC)[5]. Pulsed laser deposition of cubic MoN and WN, performed previously with identical conditions[5,19], resulted in polycrystalline MoN, which had superior crystalline quality and reduced electron losses compared to WN, albeit exhibiting positive ε_1 in the UV range, as well. So there is a solid hint that epitaxial cubic B1-MoN_x may be, indeed, a viable optical conductor and an active plasmonic material for the UV range.

Experimental and Theoretical Methods

Growth of Materials

Cubic B1-MoN_x layers were deposited on MgO(111) substrates in a loadlocked ultra-high vacuum dc magnetron sputtering system with a base pressure of $<10^{-9}$ torr as described in detail in Ref. 22. The substrates are one-side polished 10×10×0.5 mm^3 MgO wafers that were cleaned in successive rinses of trichloroethylene, acetone, isopropanol, and deionized water, blown dry with dry N_2, attached to a Mo block with silver paint, loaded into the system through a load-lock chamber, and thermally degassed at 900 ^oC for 1 h. The substrate temperature T_s was measured by a thermocouple below the sample stage that was cross-calibrated with a pyrometer focusing on the sample surface. The temperature was adjusted to the desired Ts=600-1000 ^oC prior to deposition from a 99.95%-pure 51-mm-diameter Mo target which was sputter etched before deposition for 5 min with a shutter shielding the substrate. The target was facing the substrate at a 9 cm distance and from a 45^o angle, with the substrate being continuously rotated at 60 rotations per minute to increase thickness uniformity. All depositions were done in 20 mTorr 99.999% pure N_2 and using a constant dc power of 300 W, which was applied to the magnetron for a duration of 6 min, resulting a layer

thickness ranging from 69 to 98 nm corresponding to a temperature-dependent deposition rate of 11.5-16.3 nm/min. The produced films at Ts=1000 ^{o}C were substoichiometric with x=0.69.

Optical Characterization

The optical spectra were acquired after more than one year exposure to lab atmosphere using three individual techniques, in particular: 1) a UV-Visible spectroscopic ellipsometer (SE) operating in the range 0.6-6.5 eV (2067-191 nm); measurements were acquired at 70^{o} angle of incidence and a step of 20 meV (UVISEL by Horiba Jobin-Yvon), 2) a vacuum-UV (VUV) ellipsometer (VUV-SE), operating beyond 6.5 eV up to 8 eV (155 nm) using a step of 50 meV (UVISEL 2 VUV by Horiba Jobin-Yvon), and 3) a Fourier Transform InfraRed (FTIR) spectrometer, which measures the optical reflectivity at near-normal incidence in the spectral range 5000–500 cm^{-1} (2,000-20,000 nm) with a step of 4 cm^{-1} (BRUKER FTIR-IFS113v). The FTIR spectra were normalized using a Pt reference mirror. Additional non-specular reflectivity spectra were acquired in the UV-Visible (220-850 nm) spectral range using an integrating sphere, in order to evaluate the effect of surface roughness to the optical spectra, which was found to be minor (<1.5%).

Structural and Chemical Characterization

Core-level and valence band X-ray Photoelectron Spectra (XPS) were acquired in a KRATOS Axis Ultra DLD system equipped with a monochromated AlK_{α} X-ray source, a hemispherical sector electron analyzer and a multichannel electron detector. Surface cleaning was performed by 4 nm in-situ sputter etching using a 4 keV defocused Ar^{+} beam in order to remove the native oxide from the nitride surface. The XPS measurements were acquired using 20 eV pass energy resulting in a full width at half maximum of the Ag-$3d_{5/2}$ peak of less than 500 meV. Spectral shifts due to charging of the surface were evaluated and subtracted based on the

spectral positions of the C-1s peak of adventitious Carbon and the Ar-2p peak after sputter etching. The elemental composition of the MoN_x layers was measured by Rutherford backscattering with uncertainty less than 3% as presented in Ref. 22. Raman measurements were conducted with a Horiba Lab RAM HR instrument with a 514.5 nm excitation laser.

Ab initio Calculations

For the *ab initio* calculations we followed the methodology presented in Ref. 25. In particular, we calculated the equilibrium structure, and the electron density of states (EDOS), and electron-photon and electron–phonon matrix elements for a B1-MoN supercell with one N vacancy as shown in the online supporting information (Fig, S1 left panel) using the open-source plane-wave density functional theory (DFT) software, JDFTX[26]. We use the 'PBE'[27] generalized-gradient approximation to the exchange-correlation functional, norm-conserving 'SG15'[28] pseudopotentials, a kinetic energy cutoff of 30 Eh (Hartrees) and a Fermi–Dirac smearing of 0.01 Eh. For Brillouin zone integration, we employ a Γ-centered k-point mesh with dimensions such that the effective supercell is nominally 25 Å in each direction for the electrons, while for the phonons, we use a supercell nominally 12 Å in each direction. (This amounts to 8×8×8 electronic k-point sampling for the rock-salt B1 structure).

We calculate the ε_2 spectra using Fermi's Golden rule with *ab initio* matrix elements and electronic states, employing Wannier-function interpolation to achieve accurate Brillouin zone integration with over 10^6 k-points. The intraband contributions derive fully from first principles calculations of electron-phonon scattering, from which we additionally estimate the theoretical limit on resistivity at 34 μΩ cm, indicating substantial room for further reduction of intraband losses in this material. Finally, we calculate the ε_1 spectra from ε_2 via a Kramers-Kronig integration similar to Ref. 29.

Finite Difference in Time Domain Calculations

The calculations of the optical response of the designed B1-$MoN_{0.69}$ nano-structures were performed by time-integrating Maxwell's equations on a computational grid utilizing the Finite Difference in Time Domain (FDTD) method. In the computational process the material dispersion is introduced in the form of polarization equations coupled and solved concurrently with Maxwell's equations. To accurately reproduce the optical constants of B1-$MoN_{0.69}$, within the FDTD framework, we perform a Drude-Lorentz fit to the experimental dielectric functions similar to Ref. 29. The experimental dielectric function of B1-$MoN_{0.69}$ is utilized within the FDTD framework to evaluate the plasmonic performance of B1-$MoN_{0.69}$ nanostructures. The electromagnetic fields are extracted at every point in the structure in time domain, and by applying Fourier transforms we get the corresponding quantities in frequency domain. An in-house 3D FDTD simulator[30,31] was used in all calculations. We calculate the reflection, transmission, absorption and the detailed spatial distribution of the enhanced electric fields (E-fields) for various realistic arrays of B1-$MoN_{0.69}$ nanostructures.

Results and Discussion

We investigate the optical spectra of substoichiometric (x=0.69) epitaxial cubic B1-MoN_x/MgO(111) in the wide spectral range spanning from the FUV (155 nm) to the infrared (20,000 nm), acquired by Fourier Transform InfraRed spectroscopy (FTIR), and by conventional spectroscopic ellipsometry (SE) and vacuum UV SE (VUV-SE), and we correlate them with their chemical features, and their VBEDOS. Note that the electronic and chemical features of B1-MoN_x are very sensitive to the growth temperature and only films grown at 1000 ^oC and having x<1 (=0.69) exhibit negative ε_1 in the entire FUV range; the structural and chemical features of B1-$MoN_{0.69}$ are presented in Figure 2.

The X-Ray Diffraction patterns of Figure 2a clearly show the epitaxial relation of cubic B1-$MoN_{0.69}$(111) parallel to the MgO(111) substrate; the reciprocal space mapping in the inset of Figure 2a exhibits exclusively the features of the rocksalt (B1) phase, as there is no sign of additional diffraction peaks that would be associated with other MoN_x phases with ordered vacancies[22]. Therefore, the considered epitaxial sample has the cubic B1 structure with random distribution of vacancies to accommodate the substoichiometry x=0.69. The X-ray Photoelectron Spectra of Figure 2b reveal the absence of any Mo-O bonds and an insignificant amount of adsorbed oxygen after a 4 nm surface Ar^+ etching, proving that B1-$MoN_{0.69}$ exhibits remarkable stability in terms of long-term oxidation; The Mo-$3d_{5/2}$ peak appears at the distinctive binding energy of 228.1 eV for Mo-N bonds[32]. The Raman spectrum of B1-$MoN_{0.69}$ (Figure 2c) further supports the absence of any oxide[33] contribution. The spectrum is typical of a TMN in the B1 structure and it is characterized by the pair of the transverse acoustic (TA) and longitudinal acoustic (LA) modes at low wavenumbers (<300 cm^{-1}) and the optical (O) mode at 550 cm^{-1}. The faint optical mode, compared to TA and LA, also proves a high density of defects[34], which further supports the coexistence of both anion and cation vacancies in epitaxial B1-MoN_x. The experimental VBEDOS of the conductive B1-$MoN_{0.69}$ (Figure 2d, red line) reveals its highly conductive character as there is significant accumulation of states close to the Fermi level; the VBEDOS also exhibits a well-defined peak at 6.5 eV below the Fermi level, which is assigned to the N*2p*-Mo*4d* electrons (Figure 2d, green lines)[5]; this peak proves that the *d* states of Mo are moving deep below to the Fermi level, more than any other TMN apart from B1-WN[5, 19]. The incorporation of N vacancies results in the emergence of additional states close to the Fermi level, as shown by *ab initio* calculations of VBEDOS for a B1-$MoN_{0.75}$ supercell (Figure 2d, blue line, Fig. S1 for a demonstration of the supercell) performed following the methodology of Ref. 25. These calculated spectra describe better the experimental VBEDOS of B1-$MoN_{0.69}$ in terms of the emergence of states close to the Fermi level and also explain the relatively high optical losses

due to the overlap of the intraband and interband transitions on B1-$MoN_{0.69}$, as manifested in the permittivity (ε_1, ε_2) spectra.

The experimental broadband permittivity spectra (real part ε_1, and imaginary part ε_2) of B1-$MoN_{0.69}$/MgO(111) in the range 0.6-8.0 eV (2067-155 nm) are shown in Figure 3a. The values of the real part of the permittivity ε_1 (which coincides with the dielectric function in CGS units) gets negative values in the entire experimental spectral range, providing a hint of plasmonic performance in the far UV range beyond 6.5 eV (191 nm). In order to firmly resolve the conductive character of the B1-$MoN_{0.69}$ we calculated the optical reflectivity at normal incidence *R* from the ε_1, ε_2 via the complex refractive index $\tilde{n}(\omega) = n(\omega) + ik(\omega)$ using the following equations:

$$\tilde{n}(\omega) = n(\omega) + ik(\omega) = \sqrt{\tilde{\varepsilon}(\omega)} \quad (1)$$

and

$$R(\omega) = \frac{(n(\omega)-1)^2+k(\omega)^2}{(n(\omega)+1)^2+k(\omega)^2} \quad (2)$$

Then, the VUV-SE, SE and FTIR reflectivity spectra are combined as shown in Figure 3b, where it is clearly resolved that the combined spectra in the range 155-3000 nm have the typical lineshape of the reflectivity of electron conductors. The combined reflectivity spectra were fitted in the range 155-3000 nm by a Drude-Lorentz (D2L) model, as described in Refs. 5, 6, 19, 29, 35, 36, assuming a semi-infinite B1-$MoN_{0.69}$. (*i.e.* we do not take into any substrate effects); the semi-infinite model is also consistent with the smooth surface of B1-$MoN_{0.69}$, which exhibits RMS roughness of 1.4 nm according to the X–Ray Reflectivity analysis reported in Ref. 22. In particular the model is based on the following equation for the determination of the complex dielectric function $\tilde{\varepsilon}(\omega)$:

$$\tilde{\varepsilon}(\omega) = \varepsilon_{\infty} - \frac{\omega_{pu}^2}{\omega^2 + i\Gamma_D\omega} + \sum_{j=1}^{2} \frac{f_j\omega_{0j}^2}{\omega_{0j}^2 - \omega^2 - i\gamma_j\omega} \quad (3)$$

In Equation (3) ε_{∞} is a background constant, larger than unity, which is due to high frequency contributions (beyond the experimental spectral range) referring to transitions that are not taken into account by the Lorentz term(s). The two Lorentz oscillators are located at an energy position $E_{0j}=\hbar\omega_{0j}$, with strength f_j and damping (broadening) factor γ_j. The Drude term in Equation (3) is characterized by the unscreened plasma energy $E_{pu}=\hbar\omega_{pu}$, (which is associated with conduction electron density[5, 6,19,29,35,36]) and the damping factor Γ_D, which accounts for the various electron scattering mechanisms[35-38]; for the particular case of B1-$MoN_{0.69}$ the fit renders the values E_{pu}= 9.12 eV and Γ_D=1.48 eV, that provide a resistivity value of 133 μΩ cm, which is in fair agreement with the electrically measured 250 μΩ cm; this value is at least an order of magnitude smaller than the values for WN_x[20], and comparable to the resistivity of other polycrystalline conductive nitrides[5], stoichiometric epitaxial NbN[39] and TaN[40], under-stoichiometric (x<1) epitaxial TiN_x[41] and HfN_x[42], epitaxial TiN with point defects[43], albeit higher by an order of magnitude than the resistivity of stoichiometric epitaxial TiN[41], ZrN[44], HfN[42], and VN[45].

Figure 3b shows the experimental VUV-SE (magenta line), SE (green line) and FTIR (red line) reflectivity spectra of the B1-$MoN_{0.69}$ sample, along with the result of the corresponding D2L fit (grey line). The reflectivity labeled 'D2L' corresponds to the dielectric function spectra presented in the inset of Figure 3b. The ε_1 retains negative values in the entire experimental range (155-20000 nm), while the extrapolation of the D2L fit results to wavelengths shorter than the experimental range (<155 nm) reveals that the ε_1 may retain negative values in the entire FUV range (120-200 nm). This is accompanied by positive values of ε_2, as low as 2 for 155 nm and a predicted value of 1.5 for 120 nm (Fig. 3b, inset),

thus approaching the requirements of the epsilon-near-zero (ENZ) condition in FUV range with profound implications for the design of plasmonic and photonic devices.[46-48]

Of particular importance is the origin of the negative ε_1 in the FUV range. Although B1-$MoN_{0.69}$ does have conduction electrons, revealed by the Drude component in the optical spectra (Fig. 3) and the VBEDOS (Fig. 2d), the conduction electron (Drude) components of the calculated ε_1 (Figure 4, light green line) and the experimental ε_1 (Figure 4, orange line) exhibit negative values only for wavelengths longer than 289 and 200 nm, respectively; the quantitative difference of the calculated and experimental Drude components are well understood due to the temperature difference (the calculation are performed for 0 K, while the experiment is performed at room temperature) and the absence of extended dstrtuctural defects in the computational supercell, as described previously in Ref. 29 and 35. Consequently, the observed negative values of ε_1 beyond 200 nm (grey area in Fig. 4) are the result of the contribution of interband absorption (or more precisely the defect absorption), a fact that opposes and alters our existing perception of optical conductors, according to which, the interband absorption is an undesired and deteriorating side-effect, as in the well-known cases of Au and TiN[5, 16]. Interestingly, B1-$MoN_{0.69}$ is a case where two potential plasmonic mechanisms co-exist. In visible and infrared ranges the negative ε_1 is mostly dictated by the conduction electrons and the intraband absorption, as in all mainstream optical conductors.[5,16] On the contrary, in the FUV range the defect-driven interband absorption is the origin of the negative ε_1 of B1-$MoN_{0.69}$; thus, B1-MoN_x may be considered to belong to a broader class of emerging plasmonic materials in which interband transitions play a key role to enable the negative ε_1, such as chalcogenide semiconductors[49], new Ga polymorphs[50], chalcopyrite nanocrystals[51], and semimetals and topological insulators[52], with the additional unique features of FUV plasmonic activity and defect-controlled optical absorption.

The wavelength (and photon energy) at which ε_1 becomes zero ($\lambda@\varepsilon_1=0$) is of particular technological importance, as it defines (but does not coincide with) the spectral position of LSPR[5,6]. In particular, when the $\varepsilon_1=0$ is accompanied by small positive values of ε_2 (<2), as it is shown in Fig. 5a (where the ε_1 and ε_2 raw spectra are demonstrated exclusively for the UV range with increased resolution due to the scale) the epsilon-near-zero (ENZ) condition may be well approximated and the attenuation of light is minimized, with apparent perspectives for relevant application[46-48]. Therefore, it is essential to compare the performance of B1-$MoN_{0.69}$ with the other optical conductors in terms of the wavelength at which $\varepsilon_1=0$, the value of the ε_2 at the same wavelength (the ε_2 at the wavelength where $\varepsilon_1=0$ is a quantity directly correlated with optical attenuation), and the melting point of the conductor, which is crucial for its durability to intense electric fields (either due to high photon fluxes, as in lasers, or due to high photon energies, as in UV). Such a comparison based on an extended literature survey[53-66] is presented in Figure 5b with data that are summarized in Table I. Note that the selected references are mostly for opaque, well-polished samples and, therefore, are not representative of nanostructured metals; nanostructured metals are expected to be more lossy and their performance would be less favourable compared to the presented B1-$MoN_{0.69}$. B1-$MoN_{0.69}$ clearly outperforms all TMNs and most of the metals in terms of short $\lambda@\varepsilon_1=0$, apart from Al, while it is comparable to Rh, Ru, Mg and Zn. Remarkably, B1-$MoN_{0.69}$ exhibits particularly low loss $\varepsilon_2@\varepsilon_1=0$ in the UV range, despite the existence of substantial point defects. Regarding the electron losses (estimated by $\varepsilon_2@\varepsilon_1=0$) B1-$MoN_{0.69}$ outperforms again all the competition apart from Al and Mg, albeit with the major asset over them of having remarkable thermal stability and oxidation resistance; indeed, Mo_2N oxidizes above 350 ^oC to form MoO_2 and above MoO_3 is severely oxidized due to the formation of the volatile MoO_3[67], in contrast to Al, which spontaneously oxidizes even at room temperature. It is expected that B1-MoN_x, in which the Mo is in higher oxidation state than Mo_2N to be more resistant to

oxidation; indeed, MoN was found to resist oxidation at least up to 400 ^{o}C and with partial durability up to 600 ^{o}C[68].

For practical applications and industrial implementation, the abundance of an element is also a crucial factor. Figure 5c presents the abundance of the various metals (either pure or as constituents of TMNs) in Earth's crust and their annual production rate in metric tonnes. It is apparent that Mo's abundance and production rate is higher than its major competitors for UV plasmonics, namely Ta (for TaN), Rh, Ru and Ir. Al, Zn and Mg are more abundant than Mo, but this comes in expense of their reduced thermal and chemical stability, which may be as severe as to ignite photo-explosion[69].

The potential plasmonic performance of an optical conductor may be preliminary evaluated by given figures of merit (FOM)[2]; in particular for LSPR of spherical particles[2]: $FOM = \frac{-\varepsilon_1}{\varepsilon_2}$. The FOM for B1-$MoN_{0.69}$ and the rest of the considered UV conductors are presented in Figure 5d. B1-$MoN_{0.69}$ exhibits extraordinary constant FOM values over the entire FUV range and it spectrally outperforms all the other TMNs and metals, apart from Al, Rh and Ir, which exhibit larger FOMs and consequently sharper resonances and field enhancements in the UV, albeit with the added advantages of abundance and mechanical, chemical, and thermal stability of B1-MoN_x.

In order to explore the potential of B1-$MoN_{0.69}$ as a FUV plasmonic conductor for realistic applications we employ FDTD calculations[30,31] for various nanostructures employing the complex permittivity presented in Figure 3a. We calculate the reflection, transmission, absorption and the detailed spatial distribution of the enhanced electric fields (E-fields) for various realistic arrays of B1-$MoN_{0.69}$ nanoparticles as described in the on-line supplement (Figure S3 to S7 and the corresponding text); in particular we consider the cases of free

standing nanospheres of B1-$MoN_{0.69}$, that may provide hints on the performance of hypothetical colloidal B1-MoN_x. In addition, B1-$MoN_{0.69}$ disks and cubes are model systems that would be implemented with standard lithography processes, thus, they have been chosen in order to be amenable to standard lithography technologies and their capabilities in terms of the produced feature sizes. The disks and cubes were considered as an array of free standing features, in a first effort to elucidate the resonant LSPR traits without the extra complications arising from the MgO substrate's dispersion. Note that this arrangement of nanospheres/disks/cubes is not the optimal to maximize the plasmonic response, but it is the arrangement most typically used in surface-enhanced spectroscopy applications[70-73].

Figure 6 summarizes the absorption spectra of single arrays of B1-$MoN_{0.69}$ nanostructures (more details in the on-line supplement, Figures S3 to S7). In particular, Figure 6a vividly demonstrates the effect of the shape of the nanostructures by comparing the optical absorption of free-standing cubes, spheres and disks of 20 nm. All spectra present LSPR modes at the vicinity of 140 nm (8.86 eV). This is the shortest LSPR wavelength reported in literature to our knowledge. The deepest UV response reported, so far, is at 7.5 eV for 20 nm Rh spheres in air[74]. A secondary broad absorption band is also observed in the UV range of 250-400 nm, albeit with substantially weaker resonance. Most likely the secondary long-wavelength resonance comes from the conduction electrons of B1-$MoN_{0.69}$, as lies in the same spectral region with the crossing point of the real permittivity at $\varepsilon_1=0$ of the continuous film, while the primary FUV peak is the result of the contribution of the interband absorption, as we have discussed previously. The sharpest resonance at 140 nm and the minimal secondary band are observed for the spheres, while the stronger resonance in the FUV is observed for the disks. Indeed, the insets in Figure 6a demonstrate the E-field distributions at the resonance wavelength and reveal the similarity of spheres and disks and their superiority over cubes in terms of field enhancement.

The effect of the feature size is demonstrated in Figure 6b, where the absorption spectra of free-standing arrays of 20 nm-thick disks of varying diameter (20, 40, 60 nm), but with the same surface coverage (SC) of 25%, are presented. As expected the dominant LSPR in FUV is red-shifted (from 140 to 180 nm) with increasing feature size; despite of this red-shift, the dominant LSPR is still lying in the FUV range. The FDTD calculations reveal that the detrimental side-effect of the increasing feature size is not the expected red-shift itself, but the disproportional manifestation and spectral shift of the secondary absorption band for wavelengths longer than 250 nm. Indeed, as the feature size increases, this band emerges stronger and gradually extends into the visible range. As a result, the rule of thumb for sharp resonances located exclusively in the FUV range calls for small and round features of B1-$MoN_{0.69}$. Our findings suggest that such features can be utilized for far UV applications such as FUV sensors[75] offering higher sensitivity, material selectivity and surface specificity.

As the fine nanostructures of B1-MoN_x are the best performing in the FUV range, the evaluation of the effect of oxidation to their performance is substantially important, as even minimal surface oxidation might reduce substantially the volume of the conductive phase. For these reason, FDTD calculations were performed in a B1-$MoN_{0.69}$ spherical core/MoO_3 shell structure of total diameter of 20 nm and varying shell thickness from 1 to 4 nm. The relevant optical absorption spectra and E-field distributions at the LSPR wavelength are presented in Figure 6c and the corresponding insets, respectively. Upon surface oxidation the spectral position of LSPR is weakly red-shifted from 140 nm to 160 nm, thus retaining the plasmonic performance in the FUV range. The most significant effect of surface oxidation is the weakening of the absorption band due to LSPR, possibly due to the reduction of the volume of the conductive core phase; still, even for 2 nm of surface oxidation the optical absorption due to LSPR remains significant. These results further support the durability and stability of B1-MoN_x nanostructures as FUV plasmonic components.

Conclusions

The extraordinary optical behavior of cubic B1-MoN_x (x=0.69), with ε_1 being negative and near-zero in the entire UV range, and ε_2 approaching zero, combined with DC resistivity as low as 250 μΩ cm, refractory character (B1-$MoN_{0.69}$ was grown at 1000 ^oC, so as it can sustain at least this operation temperature), mechanical stiffness, and undisputed oxidation resistance after one year, makes cubic B1-MoN_x a significant candidate to extend the use of plasmonics and photonics in the FUV (100-200 nm) spectral range. The existence of N vacancies is identified as essential for providing the distinct optical traits of B1-MoN in the ultraviolet range, as it introduces states in the EDOS that result in negative and near-zero ε_1 values in the entire UV range, a fact that opposes and alters our existing perception on the role of defects in optical conductors, according to which, the defects are an undesired and deteriorating side-effect. FDTD calculations predict that isolated B1-MoN_x nanostructures exhibit plasmonic resonances close to 140 nm with very strong absorption, and very small ε_2 values in the same spectral range. In particular, sharp and strong resonances exclusively in the FUV range are predicted for disks and spheres of 20 nm. Thus, such nanostructures provide a solid platform for durable plasmonic and photonic devices in the FUV range with great consequences for applications such as UV photocatalysis, lithographic patterning, photodetection, and hot-electron sensing.

Associated Content

The following materials are available free of charge:

Section S1: Supercell for the *ab initio* calculations of the VBEDOS and optical properties of B1-$MoN_{0.75}$

Section S2: Additional details for the analysis of the optical spectra of B1-$MoN_{0.69}$

Section S3: Comparison of B1-$MoN_{0.69}$ with other potential UV conductors

Section S4: Additional information regarding FDTD calculations

Author Information

The authors declare no competing financial interests.

Acknowledgements

This work has been financially supported by the European Union's Seventh Framework (FP7) program through the project *SMARTONICS*, Grant Agreement No. 310229, and by the U.S. National Science Foundation under Grant Nos. 1537984, 1712752, and 1629230. The VUVSE measurements have been supported by the French Government program '*Investissements d'Avenir*' managed by the National Research Agency of France (ANR) under the contract number ANR-10-EQPX-33.

References

1. Cortie , M.B., Giddings, J., Dowd, A., Optical properties and plasmon resonances of titanium nitride nanostructures. *Nanotechnology* **21**, art. no. 115201 (2010).
2. Naik *et al.* G.V., Titanium nitride as a plasmonic material for visible and near-infrared wavelengths. *Optical Materials Express* **2**, 478-489 (2012).
3. Naik, G.V., Shalaev, V.M., Boltasseva, A., Alternative plasmonic materials: beyond gold and silver. *Advanced Materials* **25**, 3264-3294 (2013).
4. Gui L. *et al.* Nonlinear refractory plasmonics with titanium nitride nanoantennas. *Nano Letters* **16**, 5708-5713 (2016).
5. Patsalas P. *et al.* Conductive nitrides: growth principles, optical and electronic properties, and their Perspectives in photonics and plasmonics. *Mater. Sci. Eng. R.* **123**, 1-55 (2017).
6. Kassavetis, S., Bellas, D.V., Abadias, G., Lidorikis, E., Patsalas, P., Plasmonic spectral tunability of conductive ternary nitrides. *Appl. Phys. Lett.* **108**, art. no. 263110 (2016).
7. S. Murai, S. *et al.* Plasmonic arrays of titanium nitride nanoparticles fabricated from epitaxial thin films. *Optics Expr.* **24**, 1143-1153 (2016).
8. Ramanathan, S., Chi, D., McIntyre, P.C., Wetteland, C.J., Tesmer, J.R., Ultraviolet-ozone oxidation of metal films. *J. Electrochem. Soc.* **150**, F110-F115 (2003).
9. Kalfagiannis, N. *et al.* Selective modification of nanoparticle arrays by laser-induced self assembly (MONA-LISA): putting control into bottom-up plasmonic nanostructuring. *Nanoscale* **8**, 8236-8244 (2016).
10. Jeong, H.-H., Mark, A.G., Fischer, P., Magnesium plasmonics for UV applications and chiral sensing. *Chem. Commun.* **52**, 12179-12182 (2016).
11. Knight, M.W. *et al.* Aluminum for plasmonics. *ACS Nano* **8**, 834-840 (2014).

12. Sanz, J.M. *et al.* UV plasmonic behavior of various metal nanoparticles in the near- and far-field regimes: geometry and substrate effects. *J. Phys. Chem. C* **117**, 19606-19615 (2013).

13. Ahmadivand, A., Sinha, R., Kaya, S., Pala, N., Rhodium plasmonics for deep-ultraviolet bio-chemical Sensing. *Plasmonics* **11**, 839-849 (2016).

14. McMahon, J.M., Schatz, G.C., Gray, S.K., Plasmonics in the ultraviolet with the poor metals Al, Ga, In, Sn, Tl, Pb, and Bi. *Phys. Chem. Chem. Phys.* **15**, 5415-5423 (2013).

15. Choi, W.S. *et al.* Dielectric constants of Ir, Ru, Pt, and IrO_2: contributions from bound charges. *Phys. Rev. B* **74**, art. no. 205117 (2006).

16. Kumar, M., Umezawa, N., Ishii, S., Nagao, T. Examining the performance of refractory conductive ceramics as plasmonic materials: a theoretical approach. *ACS Photonics* **3**, 43-50 (2016).

17. Blaber, M.G., Arnold, M.D., Ford, M.J. A review of the optical properties of alloys and intermetallics for plasmonics. *J. Phys.: Condens. Matter*. **22**, art. no. 143201 (2010).

18. Anasori, B., Lukatskaya, M.R., Gogotsi, Y., 2D metal carbides and nitrides (MXenes) for energy storage. *Nature Reviews Materials* **2**, art. no. 16098 (2017).

19. Matenoglou, G.M., Koutsokeras, L.E., Patsalas, P. Plasma energy and work function of conducting transition metal nitrides for electronic applications. *Appl. Phys. Lett.* **94**, art. no. 152108 (2009).

20. Metaxa, C. *et al.* Electronic and optical properties of rocksalt-phase tungsten nitride (B1-WN). *J. Vac. Sci. Technol. A* **35**, art. no. 031501 (2017).

21. Balasubramanian, K., Huang, L., Gall, D. Phase stability and mechanical properties of $Mo_{1-x}N_x$ with $0 \leq x \leq 1$. *J. Appl. Phys.* **122**, art. no. 195101 (2017).

22. Ozsdolay, B.D., Balasubramanian, K., Gall, D. Cation and anion vacancies in cubic molybdenum nitride. *J. Alloys Compounds* **705**, 631-637 (2017).

23. Klimashin, F.F., Koutná, N., Euchner, H., Holec, D., Mayrhofer, P.H. The impact of nitrogen content and vacancies on structure and mechanical properties of Mo–N thin films. *J. Appl. Phys.* **120**, art. no. 185301 (2016).

24. Zhang, Y. *et al.* Epitaxial superconducting δ-MoN films grown by a chemical solution method. *J. Amer. Chem. Soc.* **133**, 20735-20737 (2011).

25. Habib, A., Florio, F., Sundararaman, R. Hot carrier dynamics in plasmonic transition metal nitrides. *J. Opt.* **20**, art. no. 064001 (2018).

26. Sundararaman, R. *et al.* JDFTx: software for joint density-functional theory. *SoftwareX* **6**, 278-284 (2017).

27. Perdew, J.P., Burke, K., Ernzerhof, M. Generalized gradient approximation made simple. *Phys. Rev. Lett.* **77**, 3865-3868 (1996).

28. Schlipf, M., F. Gygi, F. Optimization algorithm for the generation of ONCV pseudopotentials. *Comput. Phys. Commun.* **196**, 36-44 (2015).

29. Matenoglou, G.M. *et al.* Optical properties, structural parameters, and bonding of highly textured rocksalt tantalum nitride films. *J. Appl. Phys.* **104**, art. no. 124907 (2008).

30. Lidorikis, E., Egusa, S, Joannopoulos, J.D. Effective medium properties and photonic crystal superstructures of metallic nanoparticle arrays. *J. Appl. Phys.* **101**, art. no. 54304 (2007).

31. Schedin, F. *et al.* Surface-enhanced Raman spectroscopy of graphene. *ACS Nano* **4**, 5617–5626 (2010).

32. Takano, I., Isobe, S., Sasaki, T.A., Baba, Y. Nitrogenation of various transition metals by N^+ ion implantation. *Appl. Surf. Sci.* **37**, 25-32 (1989).

33. Dieterle M., Mestl, G. Raman spectroscopy of molybdenum oxides part II: resonance Raman spectroscopic characterization of the molybdenum oxides Mo_4O_{11} and MoO_2. *Phys. Chem. Chem. Phys.* **4**, 822-826 (2002).

34. Chen, X.-J. *et al.* Pressure-induced phonon frequency shifts in transition-metal nitrides. *Phys. Rev. B* **70**, art. no. 014501 (2004).

35. Matenoglou, G.M. *et al.* Structure and electronic properties of conducting, ternary $Ti_xTa_{1-x}N$ films. *J. Appl. Phys.* **105**, art. no. 103714 (2009).

36. Kassavetis, S. Optical properties of $Ti_xAl_{1-x}N$ thin films in the whole compositional range. *Surf. Coat. Technol.* **295**, 125-129 (2016).

37. Kreibig, U. & Fragstein, C. The Limitation of Electron Mean Free Path in Small Silver Particles. *Zeitschrift für Physik* **224**, 307–323 (1969).

38. Patsalas, P. & Logothetidis, S. Optical, electronic, and transport properties of nanocrystalline titanium nitride thin films. *J. Appl. Phys.* **90**, 4725-4734 (2001).

39. Villegier, J.-C. *et al.* Epitaxial growth of sputtered ultra-thin NbN layers. *IEEE Transactions on Applied Superconductivity* **19**, 3375-3378 (2009).

40. Shin, C.-S. *et al.* Epitaxial NaCl structure δ-TaN_x(001): electronic transport properties, elastic modulus, and hardness versus N/Ta ratio. *J. Appl. Phys.* **90**, 2879-2885 (2001).

41. Shin, C.-S. *et al.* Growth, surface morphology, and electrical resistivity of fully strained substoichiometric epitaxial TiN_x ($0.67 \leqslant x < 1.0$) layers on MgO(001). *J. Appl. Phys.* **95**, 356-362 (2004).

42. Seo, H.-S., Lee, T.-Y., Petrov, I., Greene, J.E., Gall, D. Epitaxial and polycrystalline HfN_x ($0.8 \leqslant x \leqslant 1.5$) layers on MgO (001): film growth and physical properties. *J. Appl. Phys.* **97**, art. no. 083521 (2005).

43. Ritala, M., Leskelä, M., Rauhala, E., Haussalo, P. Atomic layer epitaxy growth of TiN thin films. *J. Electrochem. Soc.* **142**, 2731-2737 (1995).

44. Mei, A.B. *et al.* Physical properties of epitaxial ZrN/MgO(001) layers grown by reactive magnetron sputtering. *J. Vac. Sci. Technol.* **31**, art. no. 061516 (2013).

45. Mei, A.B. *et al.* Dynamic and structural stability of cubic vanadium nitride. *Phys. Rev. B* **91**, art. no. 054101 (2015).

46. Vasudev, A.P., Kang, J.-H., Park, J., Liu, X., Brongersma, M.L. Electro-optical modulation of a silicon waveguide with an "epsilon-near-zero" material. *Opt. Expr.* **21**, 26387-26397 (2013).

47. Rensberg, J. *et al.* Epsilon-near-zero substrate engineering for ultrathin-film perfect absorbers. *Phys. Rev. Appl.* **8**, art. no. 014009 (2017).

48. Maas, R., Parsons, J., Engheta, N., Polman, A., Experimental realization of an epsilon-near-zero metamaterial at visible wavelengths. *Nature Photonics* **7**, 907-912 (2013).

49. Piccinotti, D., Gholipour, B., Yao, J., MacDonald, K.F., Hayden, B.E., Zheludev, N.I., Stoichiometric Engineering of Chalcogenide Semiconductor Alloys for Nanophotonic Applications, *Adv. Mater.* **31**, art. no. 1807083 (2019).

50. Gutiérrez, Y., Losurdo, M., García-Fernández, P., Sainz de la Maza, M., González, F., Brown, A.S., Everitt, H.O., Junquera, J., Moreno, F. Gallium Polymorphs: Phase‐Dependent Plasmonics, *Adv. Opt. Mater.* **7**, art. no. 1900307 (2019).

51. Gaspari, R., Della Valle, G., Ghosh, S., Kriegel, I., Scotognella, F., Cavalli, A., Manna, L. Quasi-Static Resonances in the Visible Spectrum from All-Dielectric Intermediate Band Semiconductor Nanocrystals, *Nano Lett.* **17**, 7691-7695 (2017).

52. Toudert, J., Serna, R. Interband transitions in semi-metals, semiconductors, and topological insulators: a new driving force for plasmonics and nanophotonics, *Optical Materials Express* **7**, 2299-2325 (2017).

53. Rasigni, M., Rasigni, G. Optical constants of lithium deposits as determined from the Kramers-Kronig analysis. *J. Opt. Soc. Am.* **67**, 54-59 (1977).

54. Inagaki, T., Emerson, L.C., Arakawa, E.T., Williams, M.W. Optical properties of solid Na and Li between 0.6 and 3.8 eV. *Phys. Rev. B* **13**, 2305-2313 (1976).

55. Hagemann, H.-J., Gudat, W., Kunz, C. Optical constants from the far infrared to the x-ray region: Mg, Al, Cu, Ag, Au, Bi, C, and Al_2O_3. *J. Opt. Soc. Am.* **65**, 742-744 (1975).

56. Rodriguez-de Marcos, L. *et al.* Transmittance and optical constants of Ca films in the 4–1000 eV spectral range. *Appl. Opt.* **54**, 1910-1917 (2015).

57. Johnson, P.B. & R.W. Christy, R.W. Optical constants of transition metals: Ti, V, Cr, Mn, Fe, Co, Ni, and Pd. *Phys. Rev. B* **9**, 5056-5070 (1974).

58. Aspnes, D.E. *Handbook of Optical Constants of Solids*, E.D. Palik Ed. (Academic Press, New York, 1985).

59. Weaver, J. H., Olson, C.G., Lynch, D.W. Optical investigation of the electronic structure of bulk Rh and Ir. *Phys. Rev. B* **15**, 4115-4118 (1977).

60. Stahrenberg, K. *et al*. Optical properties of copper and silver in the energy range 2.5-9.0 eV. *Phys Rev. B* **64**, art. no. 115111 (2001).

61. Johnson, P.B. , Christy, R.W. Optical constants of the noble metals. *Phys. Rev. B* **6**, 4370-4379 (1972).

62. Werner, W.S.M., Glantschnig, K., Ambrosch-Draxl, C. Optical constants and inelastic electron-scattering data for 17 elemental metals. *J. Phys. Chem. Ref. Data* **38**, 1013-1092 (2009).

63. Rakic, A.D. Algorithm for the determination of intrinsic optical constants of metal films: application to aluminum. *Appl. Opt.* **34**, 4755-4767 (1995).

64. Golovashkin, A.I., Levchenko, I.S., Motulevich, G.P., Shubin, A.A. Optical Properties of Indium. *Sov. Phys. JETP* **24**, 1093-1099 (1967).

65. Wronkowska, A.A., Wronkowski, A., Kuklinski, K., Senski, M., Skowronski, L. Spectroscopic ellipsometry study of the dielectric response of Au–In and Ag–Sn thin-film couples. *Appl. Surf. Sci.* **256**, 4839-4844 (2010).

66. De Sande, J.C.G., Missana, T., Afonso, C.N. Optical properties of pulsed laser deposited bismuth films. *J. Appl. Phys.* **80**, 7023-7027 (1996).

67. N. Solak, N., Ustel, F., Urgen, M., Aydin, S., Cakir, A.F. Oxidation behavior of molybdenum nitride coatings, *Surf. Coat. Technol.* **174–175**, 713–719 (2003).

68. Zhu, X., Yue, D., Shang, C., Fan, M., Hou, B. Phase composition and tribological performance of molybdenum nitride coatings synthesized by IBAD, *Surf. Coat. Technol.* **228**, S184–S189 (2013).

69. Mutlu, M. *et al.* Thermoplasmonic ignition of metal nanoparticles. *Nano Letters* **18**, 1699-1706 (2018).

70. Honda, M., Kumamoto, Y., Taguchi, A., Saito, Y., Kawata, S. Plasmon-enhanced UV photocatalysis. *Appl. Phys. Lett.* **104**, art. no. 061108 (2014).

71. Kim, H., Kosuda, K.M., Van Duyne, R.P., Stair, P.C. Resonance Raman and surface- and tip-enhanced Raman spectroscopy methods to study solid catalysts and heterogeneous catalytic reactions. *Chem. Soc. Rev.* **39**, 4820-4844 (2010).

72. Anker, J.N. *et al*. Biosensing with plasmonic nanosensors. *Nature Materials* **7**, 442-453 (2008).

73. Panagiotopoulos, N.T. *et al*. Self-assembled plasmonic templates produced by microwave annealing: applications to surface-enhanced Raman scattering. *Nanotechnology* **26**, art. no. 205603 (2015).

74. Gutiérrez, Y. *et al.* The Quest for Low Loss High Refractive Index Dielectric Materials for UV Photonic Applications. *Appl. Sci.* **8**, art. no. 2065 (2018).

75. Tanabe, I. *et al.* Far- and deep-ultraviolet surface plasmon resonance sensors working in aqueous solutions using aluminum thin films. *Scientific Reports* **7**, art. no. 5934 (2017).

Table I. The data presented in Figure 5b,c,d and the references from where the optical spectra were retrieved.

Group	Material	$\lambda@\varepsilon_1=0$ (nm)	$\varepsilon_2@\varepsilon_1=0$	Melting point (ºC)	Annual production (tones) From USGS*	Abundance in Earth's crust (ppm) From USGS*	Reference
1	Li	188	0.38	180.5	35000	20	53
1	Na	238	0.1	97.72	2.55×10^8	23000	54
2	Mg	115	0.1	650	1.01×10^6	23000	55
2	Ca	282	1.19	842	N/A	41000	56
4	TiN	473	2.5	2930	6.6×10^6	5600	Epitaxial, measu-red for this work
4	ZrN	381	1.2	2980	1.46×10^6	190	Epitaxial, measu-red for this work
5	NbN	277	6.22	2573	64000	20	Epitaxial, measu-red for this work
5	TaN	363.6	6.76	3090	1100	2	29
6	MoN	108.6	0.92	1750	2.27×10^5	1.5	Epitaxial, measu-red for this work
7	Mn	245	6.5	1246	1.6×10^7	950	57
7	Re	632	17.33	3186	47.2	0.0004	58
8	Fe	552	17.3	1538	1.15×10^9	41000	57
8	Ru	115	2	2334	0.02	0.001	15
8	Os	903	11.4	3330	1	0.0001	58
9	Co	282	1.19	1495	1.23×10^5	20	57
9	Rh	110	2.5	1964	28	0.0002	59
9	Ir	150	2.5	2466	0.003	0.0003	58
10	Ni	301	8.8	1455	2.25×10^6	90	57
10	Pd	150	1.8	1554.9	208	0.0006	57
10	Pt	202	3.6	1768.3	0.172	0.003	58
11	Cu	287	5.2	1084.62	1.94×10^7	50	60
11	Ag	325	0.68	961.78	27000	0.07	60
11	Au	475	4.5	1064.18	3100	0.0011	61
12	Zn	125	1.1	419.53	1.19×10^7	75	62
13	Al	84	0.033	660.32	5.76×10^7	82000	63
13	In	250	4.5	156.6	655	0.049	64
14	Sn	200	1.8	231.93	2.8×10^5	2.2	65
14	Pb	640	14	327.46	4.82×10^6	14	64
15	Bi	280	1.5	271.3	10200	0.048	66

* Production and abundance data come from the US Geological Survey

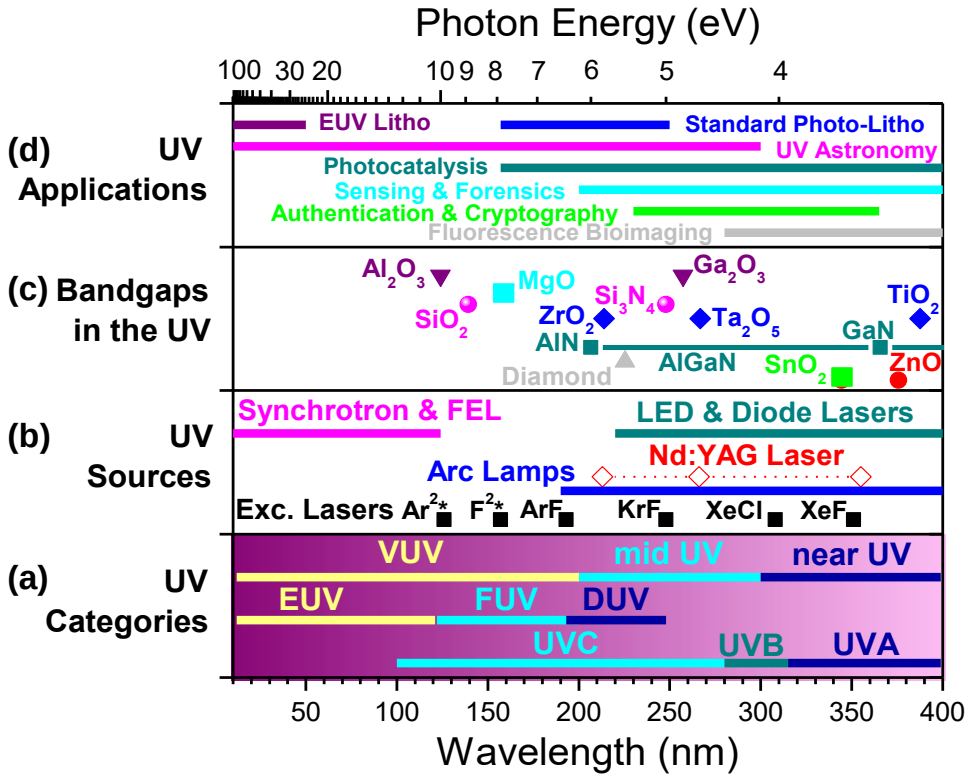

Figure 1. An overview of the UV ranges and Technologies: (a) The UV radiation can be categorized either as UVA, UVB, UVC (a terminology originating from life sciences) or near UV, mid UV and vacuum UV (VUV) or alternatively to deep UV (DUV), Far UV (FUV) and Extreme UV (UV) [terminologies originating from materials science and electronics]; the various categories are denoted in the low panel by colored bars. (b) The corresponding sources of UV radiation at various wavelengths are also shown; diode lasers, free electron lasers (FEL), Synchrotron and arc lamps provide continuous spectra, while solid-state lasers (such as Nd:YAG) and excimer lasers provide individual wavelengths. (c) A few materials can act as dielectrics or semiconductors in the UV range, mostly oxides. The $Al_xGa_{1-x}N$ family of ternary compounds is a continuous platform covering the mid UV and near UV ranges (complemented by the Ga-rich $In_yGa_{1-y}N$ family in the near UV). (d) The range of applications of UV radiation in materials science and in UV interacting with materials (*i.e.* excluding pure life science applications such as sterilization); the bars indicate the spectral extent of each technology.

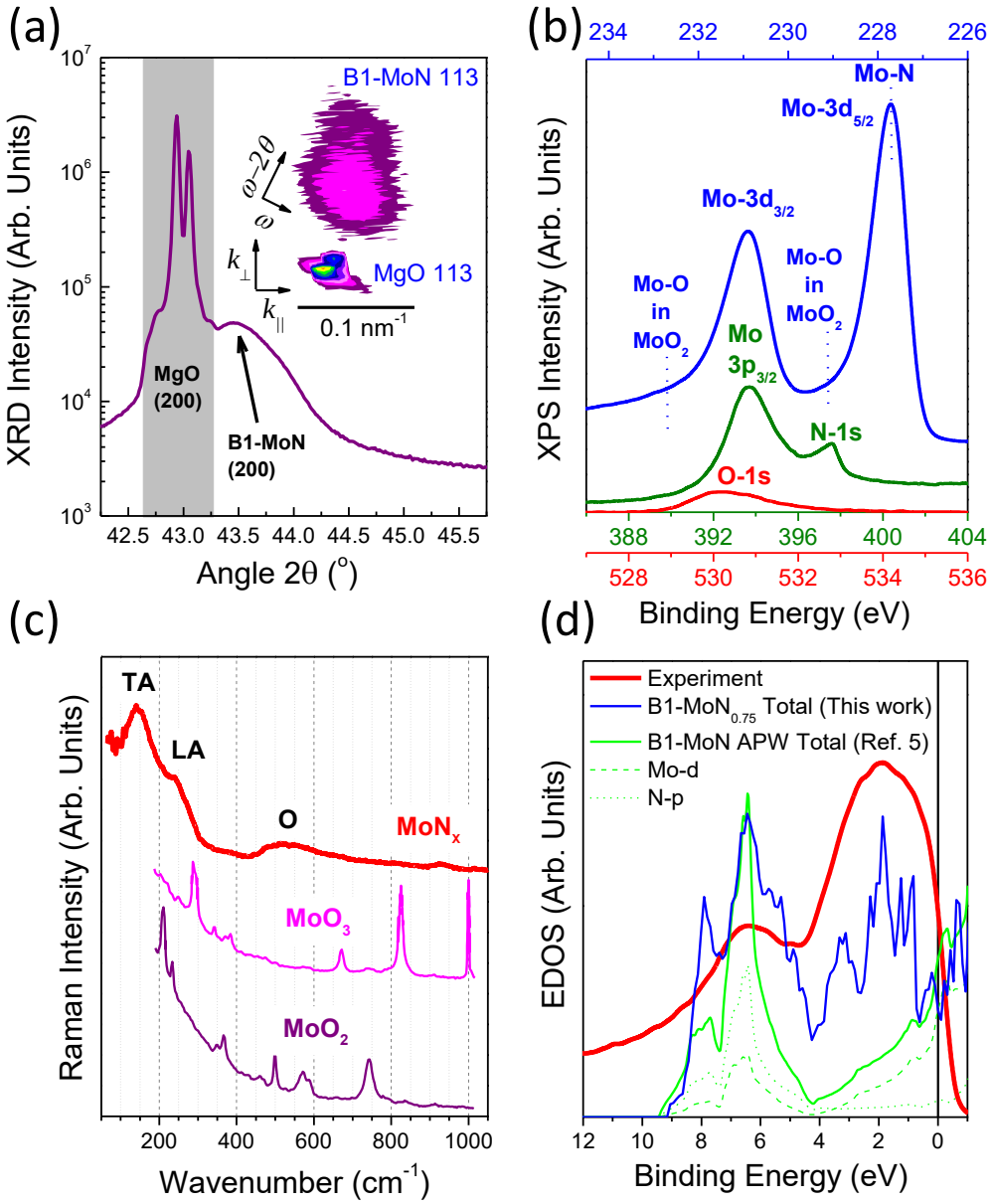

Figure 2. Structural, chemical and electronic features of cubic B1-$MoN_{0.69}$ grown at 1000 ºC: (a) XRD showing the epitaxial relation with the MgO substrate, (b) chemical analysis by XPS core levels, (c) Raman spectra revealing the absence of any oxide contribution and proving the existence of point defects, and (d) experimental (red line) and calculated by the Augmented Plane Wave (APW) method in Ref. 5 (green lines) VBEDOS confirming the B1 phase via the spectral position of the hybridized N*2p*-Mo*4d* states and the conductive character of B1-MoN_x, and the contribution of point defects calculated in this work (blue line).

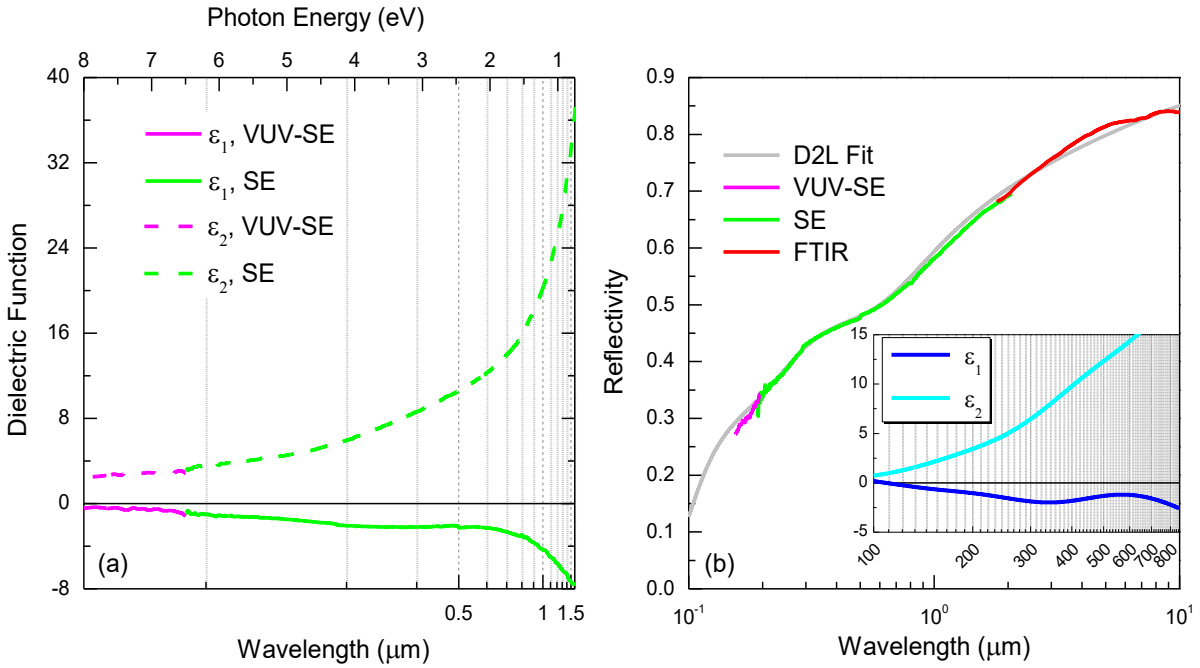

Figure 3. (a) The spectra of the real ε_1 and imaginary ε_2 parts of the dielectric function of cubic B1-$MoN_{0.69}$/MgO(111) acquired by VUV-SE and SE, (b) experimental (combined VUV-SE, SE and FTIR) and fitted reflectivity spectra of the B1-$MoN_{0.69}$ sample grown at 1000 ^{o}C. Inset: the corresponding dielectric function spectra resulted from the D2L, actual values in the range 155-850 nm and values based on the extrapolation of the fit in the 100-155 nm range.

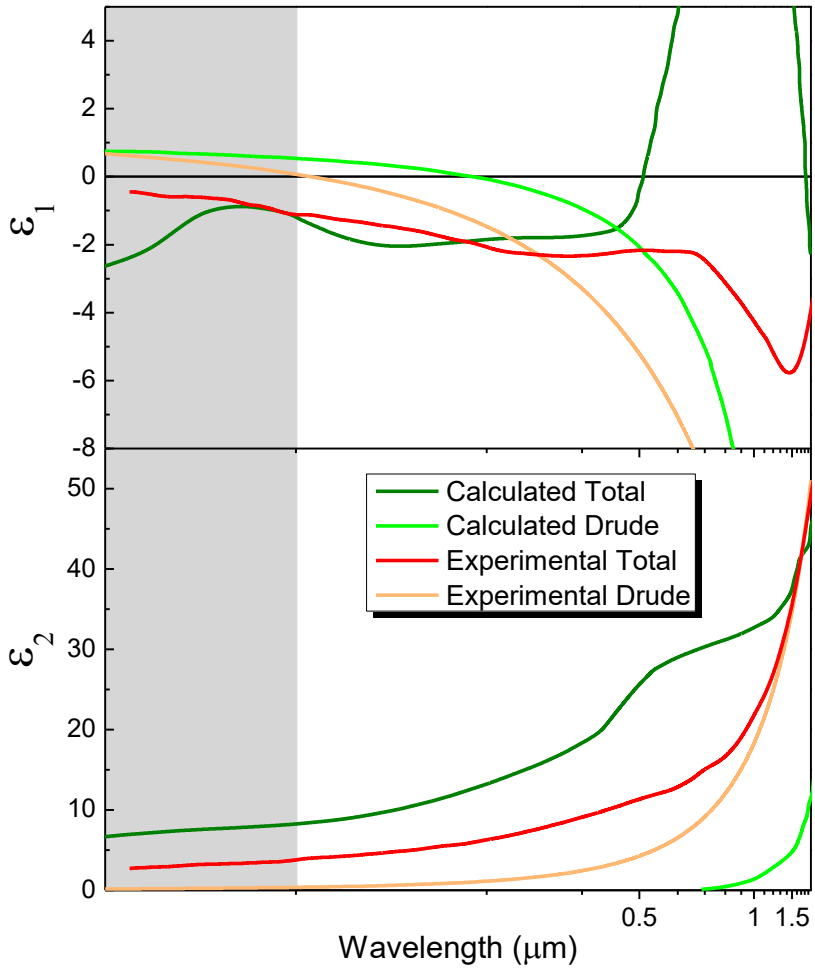

Figure 4. The real and imaginary permittivity (ε_1 and ε_2) spectra as calculated (dark green lines), with the Drude contribution alone (light green lines) and as measured (red lines), with the Drude contribution alone (orange lines).

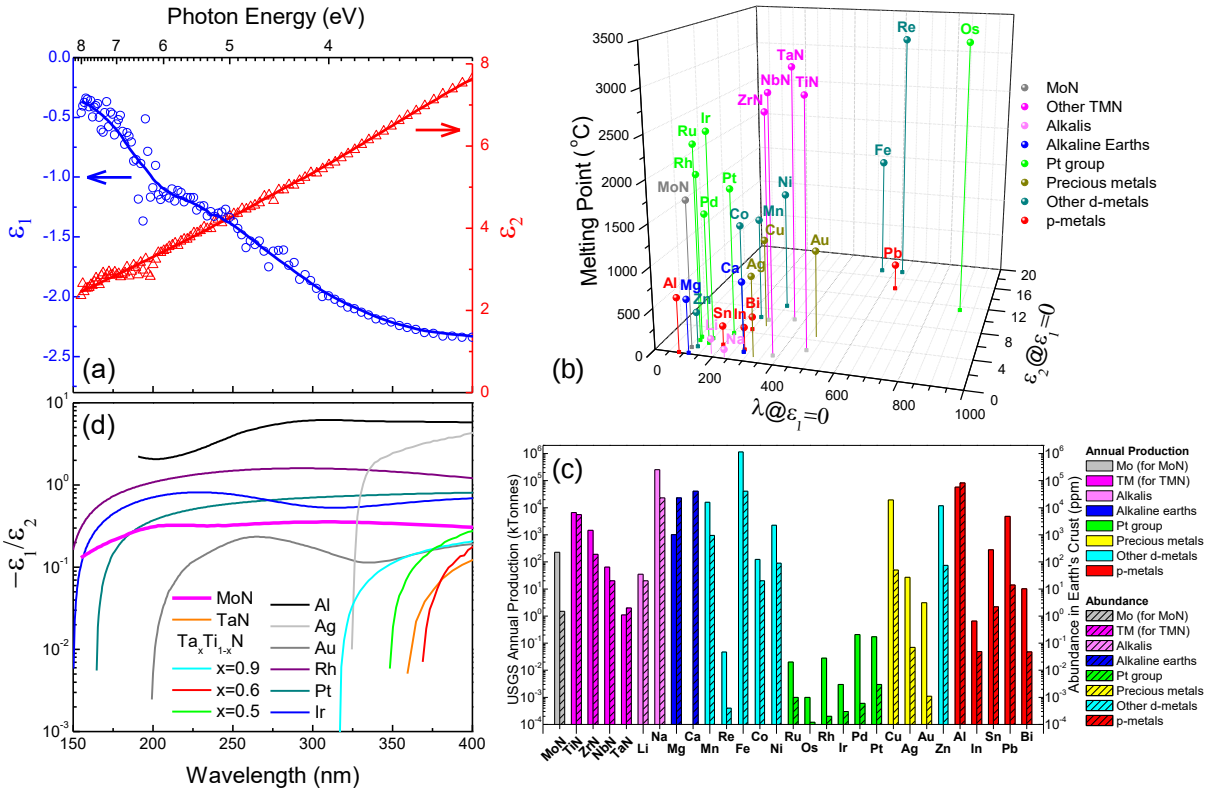

Figure 5. Comparison of B1-MoN_x with other potential plasmonic conductors: Clockwise: (a) Ellipsometry raw spectra of the real (ε_1) and imaginary (ε_2) permittivity in the UV range, (b) a critical comparison of the various candidate optical conductors in terms of $\lambda@\varepsilon_1=0$, $\varepsilon_2@\varepsilon_1=0$ and their melting point, and (c) their abundance in earth's crust and annual production according to US Geological Survey (www.usgs.gov); (d) the spectral figures of merit for LSPR for B1-$MoN_{0,69}$ (thick magenta line, denoted as MoN) along with those of the most common or promising plasmonic materials (data for TaN and $Ta_xTi_{1-x}N$ taken from Ref. 5, for the rest refer to the on-line supplement); [the wavelength and energy scales apply to both (a) and (d)].

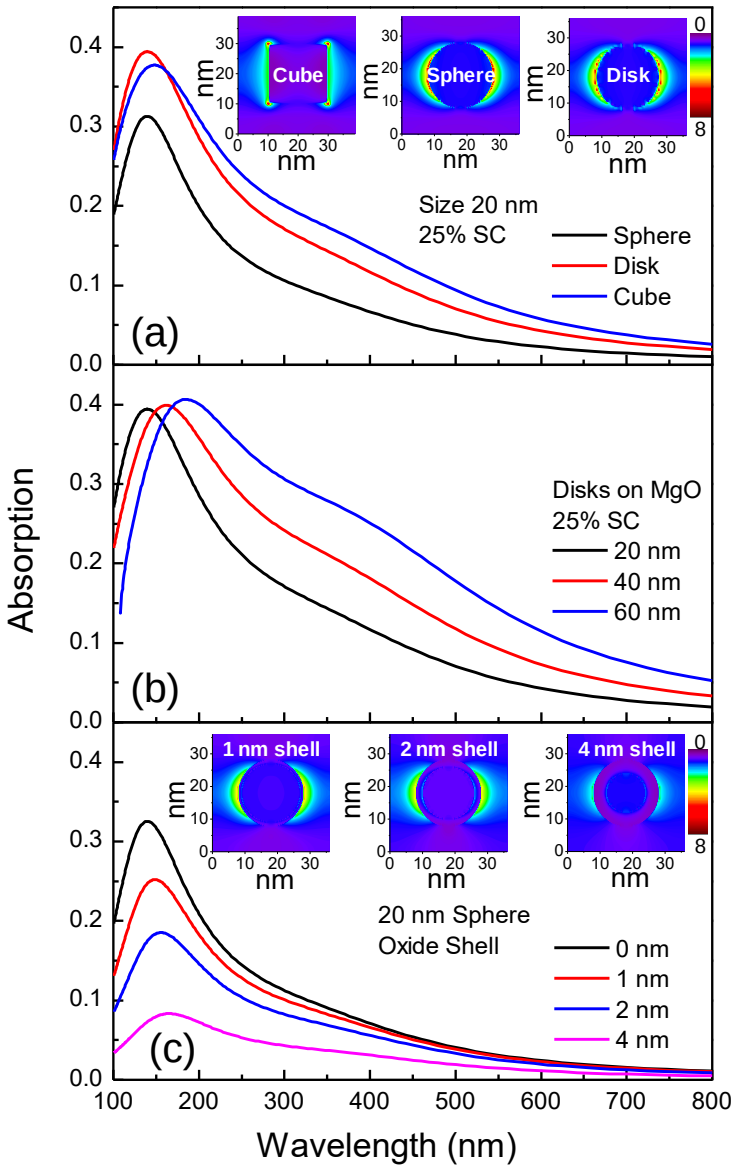

Figure 6. The potential of B1-MoN_x as a FUV plasmonic conductor: Optical absorption spectra of a single array of B1-$MoN_{0.69}$ nanostructures in air calculated by FTDT: (a) Shape effect: cubes, spheres and disks of 25% surface coverage (SC) and 20 nm size; (b) Size effect: 20 nm-thick disks of varying diameters for SC=25%, (c) Oxidation effect: 20 nm spheres for SC=25%, with varying MoO_3 oxide shells; the insets in (a) and (c) show the electric field enhancement spatial distributions at the resonance wavelength.